

Strong two-photon absorption in ErFeO_3 thin films studied using femtosecond near-infrared Z-scan technique

Cite as: J. Appl. Phys. **127**, 173104 (2020); <https://doi.org/10.1063/5.0004346>

Submitted: 11 February 2020 . Accepted: 17 April 2020 . Published Online: 06 May 2020

Anshu Gaur , Mahamad Ahamad Mohiddon , and Venugopal Rao Soma 



View Online



Export Citation



CrossMark



NEW!

Sign up for topic alerts
New articles delivered to your inbox



Strong two-photon absorption in ErFeO₃ thin films studied using femtosecond near-infrared Z-scan technique

Cite as: J. Appl. Phys. 127, 173104 (2020); doi: 10.1063/5.0004346

Submitted: 11 February 2020 · Accepted: 17 April 2020 ·

Published Online: 6 May 2020



Anshu Gaur,^{1,a)}  Mahamad Ahamad Mohiddon,²  and Venugopal Rao Soma^{3,a)} 

AFFILIATIONS

¹School of Physics, University of Hyderabad, Prof. C.R. Rao Road, Gachibowli, Hyderabad 500046, Telangana, India

²Department of Physics, SRM University, Delhi-NCR, Sonapat 131029, India

³Advanced Center of Research in High Energy Materials (ACRHEM), University of Hyderabad, Prof. C.R. Rao Road, Gachibowli, Hyderabad 500046, Telangana, India

^{a)}Authors to whom correspondence should be addressed: gauranshu20@gmail.com and soma_venu@uohyd.ac.in

ABSTRACT

Ultrafast nonlinear optical (NLO) characterization of ErFeO₃ thin films deposited by the solgel assisted spin coating technique is reported herein. In the present investigation, we have used femtosecond (fs) pulses for studying the nonlinear absorption and refraction properties of ErFeO₃ thin films. Intensity dependent open and closed aperture Z-scan experiments were performed on ErFeO₃ films in the visible and near-infrared wavelengths of 600 nm, 800 nm, and 1200 nm. To explain the observed NLO results, phenomenological models of simultaneous multi-photon and excited state absorption are developed for three-level model systems suitable for excitation wavelengths with (600 and 800 nm) and without (1200 nm) linear absorption, respectively. Optical limiting (OL) characteristic is shown to exist through the phenomenon of two-photon absorption in a certain intensity range at the three wavelengths and under the simultaneous saturation of linear absorption at 600 nm and 800 nm. The upper limit of the intensity for OL applications is demonstrated by the saturation effect. The non-linear absorption results are correlated with the linear absorption at these wavelengths, which involves electronic transitions between Fe d- and O p-orbitals.

Published under license by AIP Publishing. <https://doi.org/10.1063/5.0004346>

I. INTRODUCTION

Orthoferrites (OFs) with a chemical formula of RFeO₃ (R represents rare earth elements) are a representative of a standard magnetic system with an extremely high domain wall velocity (10⁶ m/s)^{1,2} and spin reorientation transition (SRT).³ These characteristics are unique among ferromagnetic materials. Rather, free wall-motion expresses the potential of OFs for faster data manipulation, whereas SRT (switching of an easy axis of magnetization between a axis to c axis back and forth with a change of temperature) can increase the information storage capacity. The peculiarity of OF's magnetic structure is delivered through mixed valency iron (Fe²⁺, Fe³⁺) and single valency rare earth (R³⁺) element-based two magnetic subsystems. The magnetic ordering in RFeO₃ occurs through R-R magnetic moment interaction at very low temperatures, whereas room temperature magnetism is brought by iron

moments. It is shown by De Jong⁴ and Kimel *et al.*⁵ that the spin dynamics of OF-magnets can be tuned by the inverse Faraday effect by the interaction with ultrashort laser pulses.⁶ The switching time of the domains, as a result of such an interaction, is reduced to few picoseconds, which is considered as another step forward in the direction of utilizing OFs for faster magnetic data manipulation. Later on, a number of studies were performed on the characterization of laser induced spin dynamics of ErFeO₃, TmFeO₃, and other orthoferrites.^{6,7} RE-orthoferrites, especially TbFeO₃, YFeO₃, and ErFeO₃ are though subjected to ultrafast laser pulses (at low temperatures), yet no work has been reported to assess the nonlinear optical (NLO) properties of these materials to the best of our knowledge. A similar perovskite, orthochromites YCrO₃^{8,9} is shown to have two-photon assisted excited state absorption with nanosecond laser pulses at 532 nm excitation wavelength (λ_{exc}).

Materials with well-defined and strong NLO characteristics have revolutionized the field of laser and optics and formed ground of many modern days' technologies such as ultrafast optics, ultrashort lasers, photonics, and optoelectronics. Depending upon whether materials' absorption increases or decreases with the intensity, two kinds of NLO effects, respectively, are classified, (1) reverse saturable absorption (RSA) suited to optical limiting, pulse shaping applications^{10–12} and (2) saturable absorption materials useful for mode locking applications.^{13,14} The present work deals with the intensity and wavelength dependent study of NLO characteristics of ErFeO₃ films deposited on the quartz substrate under the irradiation of femtosecond laser pulses in the standard Z-scan technique. Phenomenological models of non-linear absorption (NLA) including the saturation suitable at these wavelengths are developed and applied to estimate the NL absorption and refraction parameters. For example, open aperture Z-scan spectra of ErFeO₃ at 800 nm are the attribute of linear and NL (two-photon) absorption, which at higher input power is shown to saturate. A wider scope of the material is searched by intensity and wavelength dependent characterizations.

II. MATERIALS AND METHODS

ErFeO₃ films with a thickness of $\sim 1 \mu\text{m}$ were deposited by the solgel assisted spin coating technique. The ErFeO₃ precursor sol was prepared using high purity nitrates, erbium nitrate pentahydrate [Er(NO₃)₃ · 5H₂O, metals basis], and iron (III) nitrate nonahydrate [Fe(NO₃)₃ · 9H₂O]. Acetone and 2-methoxy ethanol were used as solvents. Stoichiometrically weighed erbium nitrate pentahydrate and iron nitrate nonahydrate were dissolved in acetone and 2 methoxy ethanol solvents, respectively, at 80 °C on a magnetic stirrer. These two dissolved solutions were mixed drop by drop with a constant stirring. The pH value of the solution during the mixing was maintained between 2 and 3 by adding diethylamine. The resulting solution was cooled down to room temperature and then kept for stirring for 24 h. This sol was used to prepare ErFeO₃ thin films by the spin coating technique. ErFeO₃ thin films were coated on a quartz substrate at 3000 rpm for 1 min. These coated films were subjected to heat treatment at 100 °C for 2 h in a hot air oven to remove the residual solvents. Then, the films were heat treated at 350 °C for 1 h to remove the organic materials. Annealing was carried at 700 °C for the duration of 2 h. The thickness of the film was measured by a surface profilometer (Ambios Tech., USA, Model XP-1). The structural characterization of the deposited films was carried out using an x-ray diffractometer (Bruker Model: D8 Discover) and micro-Raman spectroscopy (WiTec Germany, Model alpha 300). The x-ray diffractograph was recorded in the grazing incident geometry with Cu $\kappa\alpha$ radiation, incident on the film sample at an incidence angle of 0.5°. The Raman spectra of the ErFeO₃ thin film were recorded in air using Nd-YAG laser at 532 nm in the backscattering geometry. A 100× objective was used to focus the sample and a Peltier cooled detector was used to record the Raman spectra. Linear absorption properties of ErFeO₃ thin films were investigated in the wavelength range of 200–1100 nm using a double beam UV-Visible spectrophotometer (JASCO model V-570). Atomic force microscopy measurements were carried in a contact mode using microscopy in a special configuration (WiTec Germany, Model alpha 300).

Nonlinear refraction (NLR) and absorption properties of ErFeO₃ thin films are characterized in closed and open aperture Z-scan configurations, respectively. The Z-scan experiments at 800 nm were performed with a Ti-Sapphire pulsed laser beam (pulse width: 50 fs, repetition rate: 1 kHz). The amplifiers were seeded with ~ 15 fs pulses from the oscillator (Coherent, Micra). The femtosecond pulses at wavelengths of 600 and 1200 nm were derived from an optical parametric amplifier (Light conversion, TOPAS) operating at 1 kHz and with the above mentioned Ti-Sapphire laser at its input. In the experimental arrangement, 3 mm diameter laser beam was focused to the $1 \mu\text{m}$ thin film sample (deposited on a quartz substrate) using a plano-convex lens of 15 cm focal length. The transmitted light was collected by a photodetector (Si photodiode, SM1PD2A, Thorlabs) connected with a lock-in-amplifier set to detect a signal of 1 kHz. The sample was placed on a motorized sample stage that can move (0.25 mm/step, 0.5 mm/step) in the beam direction (i.e., Z direction). The automated sample stage and the photodiode are interfaced together through LabVIEW programming on a computer. The schematic and other details of the Z-scan experimental arrangement are presented elsewhere.¹⁵ Input intensity dependent NLO characterization was performed at the wavelengths of 600 nm (2.07 eV), 800 nm (1.55 eV), and 1200 nm (1.03 eV).

III. THEORETICAL BACKGROUND

The closed aperture (CA) Z-scan data which characterize the NLR properties of ErFeO₃ were fitted with the standard relation for transmittance derived by Sheik-Bahae *et al.*¹⁶ The relation is developed by solving the Lambert Beer-type differential equations for phase shift $\Delta\varphi$ and the transmitted intensity I from the sample, given as

$$\frac{d\Delta\varphi}{dz'} = \Delta n(I)k, \quad (1)$$

$$\frac{dI}{dz'} = \alpha(I)I, \quad (2)$$

where z' is the sample penetration depth, Δn is an intensity dependent part of the refractive index, and α is the total absorption coefficient of the sample which, in general, contains linear and NL contribution. Equations (1) and (2) when solved for $\Delta\varphi$ under the constraint of cubic nonlinearity and no NLA results to on-axis phase shift at the focus and Z-scan transmittance at the exit surface of the sample as

$$\Delta\varphi_0(t) = k\Delta n_0(t)L_{\text{eff}}, \quad (3)$$

$$T = 1 - \frac{4 \frac{z}{z_R} \Delta\theta_0}{\left(1 + \left(\frac{z}{z_R}\right)^2\right) \left(9 + \left(\frac{z}{z_R}\right)^2\right)}, \quad (4)$$

where $\Delta n_0(t) = n_2 I_{00}(t)$ with $I_{00}(t)$ being the on-axis intensity at the focus, $k = 2\pi/\lambda$ is the wave vector, $L_{\text{eff}} = (1 - e^{-\alpha_0 L})/\alpha_0$ is

known as the samples' effective length α_0 being the linear absorption coefficient, L the sample's actual length. CA data are fitted using Eq. (4) treating $\Delta\varphi_0$ as a fit parameter.

The open aperture (OA) Z-scan data are fitted by solving Eq. (2) for sample thickness $z'=L$ with α containing terms of linear, multiphoton, and excited state absorptions (Fig. 1),

$$\alpha(I) = \alpha_0 + \beta I + \gamma I^2 + \alpha_1 + \alpha_2, \quad (5)$$

where α_0 , β , and γ are the linear, two- and three-photon absorption coefficients, α_1 and α_2 are excited state absorption (ESA) coefficients corresponding to the transitions from S_1 (band) to S_2 (band) and from S_2 (band) to S_3 (band), respectively. Equation (2) is solved at different sample positions (Z-values) with $I_{00}/[1 + (z/z_R)^2]$ as the input intensity, where z_R is the Rayleigh length ($=\pi w_0^2/\lambda$). Equation (5) in its current form is valid, when all the processes occur without any saturation effect and are independent of each other, which are the case only at lower intensities and large total population density; in general, it is not valid. General expressions for NLA coefficients are obtained by solving the rate equations for the population at different energy states. Various possible transitions applicable to ErFeO_3 in the four-level model system are depicted in Fig. 1. The rate equations at S_3 , S_2 , S_1 , and S_0 states are given as

$$\frac{dN_3}{dt} = \frac{\gamma I^3}{3(hv)^2} + \frac{\sigma_{E23}N_2I}{hv} - \frac{N_3}{\tau_3}, \quad (6)$$

$$\frac{dN_2}{dt} = \frac{\beta I^2}{2hv} - \frac{N_2}{\tau_2} + \frac{\sigma_{E12}N_1I}{hv} - \frac{\sigma_{E23}N_2I}{hv} + \frac{N_3}{\tau_3}, \quad (7)$$

$$\frac{dN_1}{dt} = \frac{\sigma_1(N - N_1 - N_2 - N_3)I}{hv} - \frac{N_1}{\tau_1} - \frac{\sigma_{E12}N_1I}{hv} + \frac{N_2}{\tau_2}, \quad (8)$$

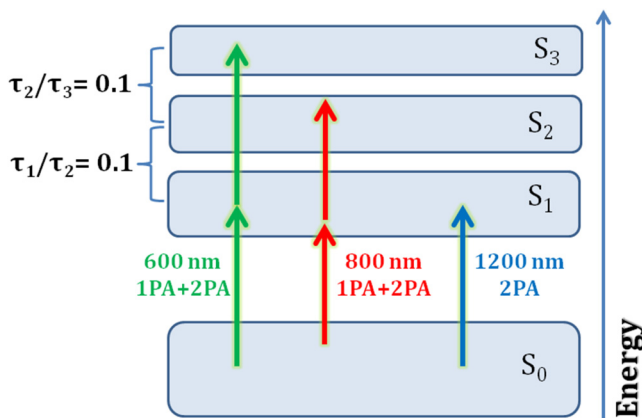


FIG. 1. Four-energy level model for an ErFeO_3 material system. The possible transitions during excitation by femtosecond laser pulses of 600 nm (left), 800 nm (middle), and 1200 nm (right) wavelengths are shown by vertical arrows.

$$\frac{dN_0}{dt} = -\frac{\sigma_1(N - N_1 - N_2 - N_3)I}{hv} - \frac{\beta I^2}{2hv} - \frac{\gamma I^3}{3(hv)^2} + \frac{N_1}{\tau_1}, \quad (9)$$

where N_0 , N_1 , N_2 , and N_3 are the population densities (No. of molecules/cm³) at the S_0 (ground state), S_1 , S_2 , and S_3 bands respectively, N is the undepleted population density of ErFeO_3 , h is Planck's constant, ν is the frequency of the light, τ_1 , τ_2 , and τ_3 are the relaxation times at the S_1 , S_2 , and S_3 bands, respectively, σ_1 , σ_{E12} , and σ_{E23} are the linear, ESA cross sections for S_1 to S_2 and S_2 to S_3 transitions, respectively. These equations are solved for N_1 , N_2 , and N_3 under the steady state condition (i.e., $dN_i/dt = 0$, $i = 1, 2$, and 3). Obtained populations are substituted in Eqs. (10)–(13) and then in (5),

$$\beta = \sigma_{2PA}(N - N_1 - N_2 - N_3)/h\nu, \quad (10)$$

$$\gamma = \sigma_{3PA}(N - N_1 - N_2 - N_3)/(h\nu)^2, \quad (11)$$

$$\alpha_1 = \sigma_{E12}N_1, \quad (12)$$

$$\alpha_2 = \sigma_{E23}N_2. \quad (13)$$

Depending upon whether LA is significant or insignificant at the chosen wavelengths, Eq. (5) is simplified to the one describing three NL phenomena maximum at a time. For example, for the case of 1200 nm where LA is negligibly small [Fig. 2(d)], the rate equation corresponding to 1PA or N_1 is not included since S_1 will remain almost unpopulated (i.e., $N_1 = 0$) over a long period of time. The final form of absorption coefficients for 600–800 nm ($\alpha_0 \neq 0$) and 1200 nm ($\alpha_0 = 0$) cases are obtained as

$$\alpha_{600,800}(I) = \frac{\alpha_{00} + \beta_0 I + \alpha_{E12} \left[\frac{I}{I_{S1}} + \eta_{12} \left(\frac{I}{I_{S2}} \right)^2 \right]}{1 + \left(\frac{I}{I_{S1}} \right) \left(1 + \eta_{12} \frac{I}{I_{SE1}} \right) + \left(\frac{I}{I_{S2}} \right)^2 \left(1 + \eta_{12} + \eta_{12} \frac{I}{I_{SE1}} \right)}, \quad (14)$$

$$\alpha_{1200}(I) = \frac{\beta_0 I + \gamma_0 I^2 + \alpha_{E23} \left[\left(\frac{I}{I_{S2}} \right)^2 + \eta_{23} \left(\frac{I}{I_{S3}} \right)^3 \right]}{1 + \left(\frac{I}{I_{S2}} \right)^2 \left(1 + \eta_{23} \frac{I}{I_{SE2}} \right) + \left(\frac{I}{I_{S3}} \right)^3 \left(1 + \eta_{23} + \eta_{23} \frac{I}{I_{SE2}} \right)}, \quad (15)$$

where I_{S2} , I_{S3} , and I_{SE} are referred to as the saturation intensities for 2PA, 3PA, and ESA processes, respectively, whose forms are given as $I_{S1} = h\nu/\sigma_{1PA}\tau_1$, $I_{S2} = \sqrt{2(h\nu)^2/\sigma_{2PA}\tau_2}$, and $I_{S3} = \sqrt[3]{3(h\nu)^2/\sigma_{3PA}\tau_3}$, $I_{SE1} = h\nu/\sigma_{E12}\tau_2$, $I_{SE2} = h\nu/\sigma_{E23}\tau_3$, and $\eta_{12} = \tau_1/\tau_2$, $\eta_{23} = \tau_2/\tau_3$ with σ_s and τ_s being the absorption cross sections and lifetime of the excited states, respectively. From Eqs. (14) and (15), it is clear that the three processes, 2PA, 3PA, and ESAs, are coupled to each other in contrast to the models reported in the literature.^{17–19} Furthermore, in the case of negligible 3PA, negligible ESA which is certainly the case of short-lived pulse (e.g., fs) excitation compared

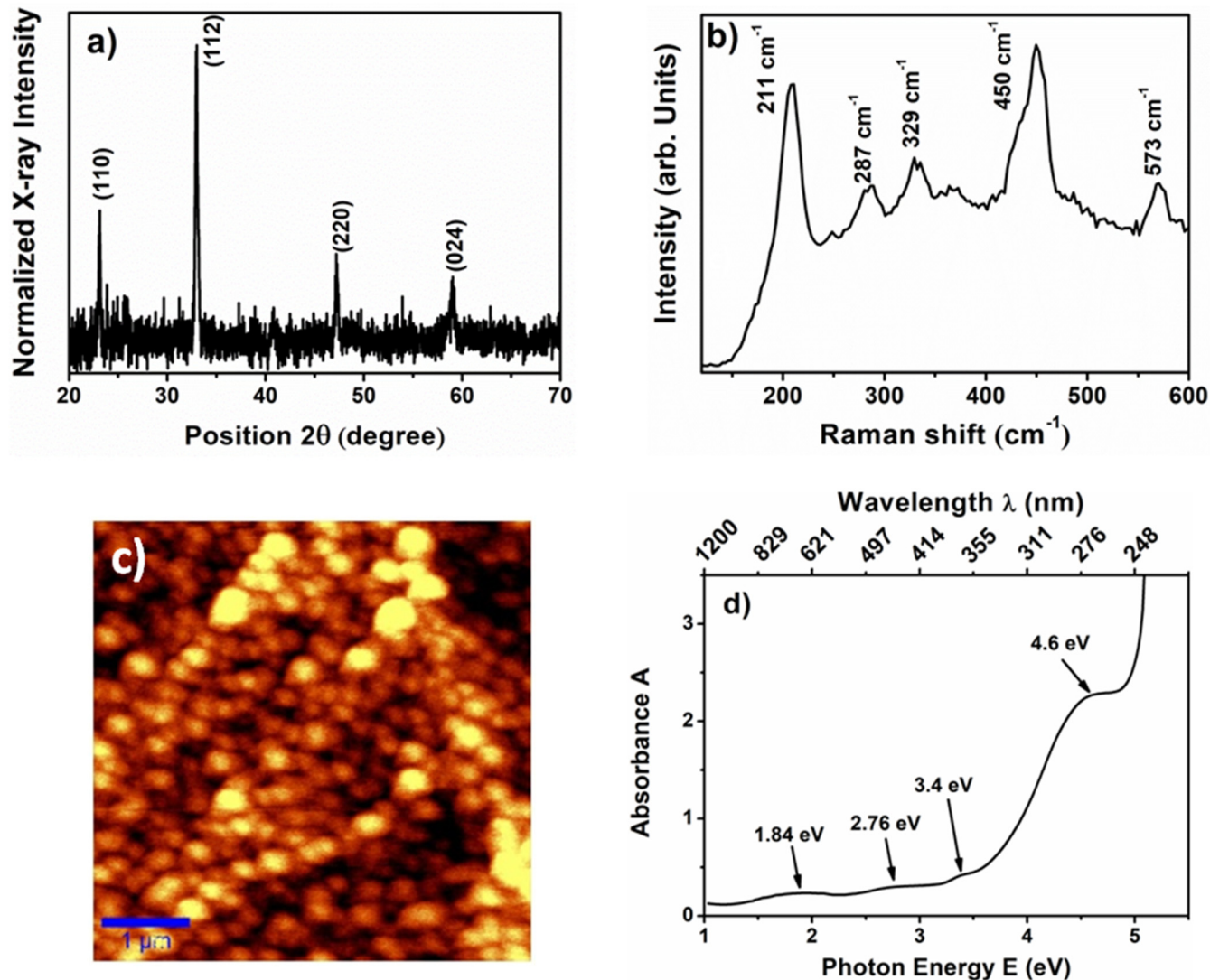


FIG. 2. (a) X-ray diffractogram, (b) Raman spectrum, and (c) AFM image, and (d) absorption spectrum of solgel assisted spin coated ErFeO_3 film.

to relaxation time of ESs (\approx ps or ns)^{9,20} and α_{E12} , $\alpha_{E23} = 0$ and I_{SE1} , $I_{SE2} \gg I$ above expressions are reduced to simpler forms as

$$\alpha_{600,800}(I) = \frac{\alpha_{00} + \beta_0 I}{1 + \frac{I}{I_{S1}} + \left(\frac{I}{I_{S2}}\right)^2 (1 + \eta_{12})}, \quad (16)$$

$$\alpha_{1200}(I) = \frac{\beta_0 I}{1 + \left(\frac{I}{I_{S2}}\right)^2}. \quad (17)$$

The form of α in Eq. (16) governing the saturation of 1PA and 2PA is different from those reported in the literature.^{17–19} In the limiting cases when β_0 is negligibly small and $I \ll I_{S2}$, it is reduced to $\alpha_{00}/(1 + I/I_{S1})$ and to $\beta_0 I/[1 + (I/I_{S2})^2]$ when there is no LA at λ_{exc} ($\alpha_{00} \approx 0$) and $I \ll I_{S1}$. The latter is nothing but Eq. (17) for pure 2PA. The linear and 2PA saturation processes for a homogeneously broadened system are reported to be governed by models containing denominator terms¹⁹ of $[1 + I/I_S]$ and $[1 + (I/I_S)^2]$ and for an inhomogeneously broadened system, $[\sqrt{1 + I/I_S}]$ ¹⁷ and $[\sqrt{1 + (I/I_S)^2}]$,^{17,18} respectively. These forms are derived for the systems involving a single process of either of 1PA or 2PA, etc. Adding the above terms to explain the complex Z-scan graphs or to include the concurrently occurring absorption processes^{15,17,21–24}

is merely an oversimplification. It is because under the multiple absorption situations the laser beam of intensity, I , or the photons simultaneously will be available for all the processes. In a similar way, the total number of molecules, N , will be distributed over each process of absorptions.^{20,25,26} In a specific comparison, the absorption model presented by Rangel-Rojo *et al.* appears in a close relation, however is not exactly the same, with the one developed in this paper. Rangel-Rojo *et al.* have developed the model for simultaneous 1PA and ESA processes in terms of absorption cross section and not in terms of absorption coefficient. Also, the saturation intensity parameter ($I_S = hv/\sigma_{1PA}\tau_{21}$) is defined only for one of the processes, i.e., 1PA. If in their equation σ_r ($=\sigma_{ESA}/\sigma_{1PA}$), τ_r ($=\tau_{32}/\tau_{21}$) and I_S terms are replaced with their definitions, provided in the literature, we will not reach to Eq. (14) modified with $\beta_0 = 0$ and $I_{S2} \gg I$. This difference occurred because of the way the population density has been considered, while writing the rate of population increase at the FES and SES. The absorption is proportional to the instantaneous population at the lower energy state. In our view, if the instantaneous population at the GS, FES, and SES are assumed to be defined by N_0 , N_1 , and N_2 , respectively, such that $N = N_0 + N_1 + N_2$ is a constant, the 1PA coefficient or cross section should be proportional to $N_0 = N - N_1 + N_2$ and not $N_0 - N_1$ because such a change of population is already being considered in its instantaneous-type definition of N_0 , N_1 , and N_2 . One has to check that what changes it may cause in the estimated absorption parameters. However, it is not the focus of the present work. Finally, Eq. (2) can be solved for intensity I by treating β_0 and I_{S2} as fit parameters if η_{12} are known by the experiment or the literature.

IV. RESULTS AND DISCUSSION

A. Synthesis and structural characterization

The crystalline phase of the 1- μm thick ErFeO_3 thin film was confirmed through x-ray diffraction data. The XRD data of the ErFeO_3 film measured in the grazing incident geometry mode are shown in Fig 2(a). The diffractograph in the figure contains a set of four XRD peaks impregnated on a high background. The four visible peaks at 23.14° , 32.99° , 47.27° , and 59.16° correspond to (110), (112), (220), and (204) planes of an orthorhombic structure belonging to a Pnma space group (JCPDS file No. 001-074-1480). Using the peaks position and (hkl)-indices, lattice parameters are calculated to be $a = 5.26 \text{ \AA}$, $b = 5.58 \text{ \AA}$, and $c = 7.59 \text{ \AA}$, which are found to be consistent with the reported values.²⁷ The absence of any peak at $\sim 30^\circ$ and $\sim 61^\circ$ discards the presence of a hexagonal phase, which is another possible structure for rare-earth ferrites.^{28,29} The lattice strain developed during the deposition of the film is estimated by comparing the XRD peak position of the recorded pattern and the standard powder diffraction data given in the JCPDS database using the relation, Lattice strain $= \frac{(d_{\text{obs}} - d_{\text{ref}})}{d_{\text{ref}}} \times 100$, where d_{obs} and d_{ref} are the interplanar spacing of the ErFeO_3 sample and the reference corresponding to maximum intensity peak, i.e., (112). The strain is estimated to be +0.62% and positive sign of it represents its tensile nature. Such a low level of strain in the deposited ErFeO_3 film is due to the amorphous nature of the substrate and relatively good thickness of the film. From the width of a strong XRD

(112)-peak, the average crystallite size is calculated using Debye-Scherrer's equation and is found to be 73 nm.

The Raman spectra of ErFeO_3 film annealed at 700°C for 2 h are presented in Fig. 2(b). There are five strong Raman active modes observed in the range of 200 cm^{-1} to 600 cm^{-1} , with no Raman active modes below 200 cm^{-1} . Before, we will be able to associate these modes with any of the specific vibration of ErFeO_3 , it is required to review the structure and Raman spectra details available in the literature. A detailed study^{30,31} on the Raman spectra has been reported at low temperatures, wherein Raman shift mostly was below 200 cm^{-1} . These peaks are the results of Raman scattering from magnon excitations and occur by the fluctuations in spin magnetic moments of rare earth ions.^{30,31} These scattering studies on RFeO_3 follow from its characteristic magnetic phenomena, e.g., spin reorientation, exhibited as a result of competition between thermal and anisotropy energies.³¹ On the other side, limited reports are available on the Raman scattering from phonon modes.^{32,33} It is known that ErFeO_3 in a weakly distorted perovskite structure belonging to the space group of D_{2h} ¹⁶ or $Pnma$ ³⁴ contains four formula units per unit cell, with R (=Er) atom occupying at the center of distorted octahedra formed by the oxygen atoms. Due to this, the normal phonon modes decompose and, in phonon mode representation, these modes at the center of the Brillouin zone are given by³¹ $\Gamma = 7A_{1g} + 8A_{1u} + 7B_{1g} + 8B_{1u} + 5B_{2g} + 10B_{2u} + 5B_{3g} + 10B_{3u}$. Among these modes, 24 are Raman active vibrational modes, 28 are infrared vibrational modes, and 8 are inactive modes.³² These 24 Raman active modes belong to the irreducible representation of $7A_{1g}$ (xx, yy, zz), $7B_{1g}$ (xy, yx), $5B_{2g}$ (zx, xz), and $5B_{3g}$ (yz, zy) given by³⁵ $\Gamma_{\text{Raman}} = 7A_{1g} + 5B_{1g} + 7B_{2g} + 5B_{3g}$. The Raman modes depicted in Fig. 2(b) recorded at room temperature are related to the rotation and stretching operation associated with the lighter oxygen atom in the FeO_6 octahedra. The occurrence of modes in different ranges follows the fact that the lighter atoms have a high frequency mode compared to the heavier atoms. Weber *et al.* have carried out density functional theory calculations of phonon modes in rare-earth orthoferrites and assigned the vibrational pattern to each mode.³³ Similar reports were published in the literature about the Raman spectra of RE ferrites including ErFeO_3 , which have assigned the vibrational mode of orthoferrites³⁰⁻³². These modes are tabulated in Table I along with the experimentally observed data reported in Fig. 2(b). All the data reported in the literature were recorded on single crystals and so the measurements of the polarized Raman scattering were well controlled. However, in the present investigation, RE ferrite films were grown on an amorphous quartz substrate. The Raman scattering measurements were also performed in a typical configuration without any polaroid setup. Furthermore, the difference in the Raman modes position from the reported ones is expected to be due to the strain that develops in the film, which alters the bond strengths of the ErFeO_3 unit cell. A shift in the mode position to the higher wave number side basically indicates an increase in the force constant of the bond. From the Raman spectra investigation, we confirmed that the ErFeO_3 films are in the orthorhombic structure, which supports the observations found in x-ray diffraction measurements.

The quality of the ErFeO_3 thin film surface was investigated by recording the morphology of the film by an atomic force microscope (AFM). Figure 2(c) depicts the AFM micrograph of the ErFeO_3 thin film annealed at 700°C for 2 h. A uniform grain

TABLE I. Different phonon modes of ErFeO₃.

| Symmetry | Reported theoretical mode (cm ⁻¹) ³¹ | Main atomic motion ³³ | Experimental mode (cm ⁻¹) |
|-----------------------------------|---|--|---------------------------------------|
| A _{1g} | ... | [010] _{pc} FeO ₆ rotation in phase | 211 |
| A _{1g} | 273 | O(1) x-z plane | 287 |
| B _{1g} | 322 | [010] _{pc} FeO ₆ rotation out of phase | 329 |
| A _{1g} | 434 | Fe-O(2) stretching, in phase | 450 |
| A _{1g} , B _{1g} | 505 | Fe-O(1) stretching | 573 |

distribution throughout the film surface was observed. Grains are densely packed without visible voids and porosity over the entire surface of the sample. A line across the micrograph is drawn. From the data of line profile, average grain distributed and roughness are calculated and found to be 410 nm and 18 nm, respectively. For the film deposited by the solgel assisted spin coating technique, 18 nm roughness is considered as relatively good quality of the film.

The structural identity was further confirmed by the absorption spectra analysis of the spin coated ErFeO₃ thin film. The two possible phases, hexagonal and orthorhombic, exhibit fairly different absorption characteristics.²⁸ Figure 2(c) shows the absorption spectrum of the ErFeO₃ film as a function of photon energy (1 eV–5.5 eV) and wavelength (200–1200 nm). The absorption tendency represented by the absorption coefficient is significantly higher in the UV region compared to those in the Vis or IR region. The spectrum is characterized by a strong absorption peak at 4.6 eV along with three small humps in <4 eV-region. The spectrum after de-convolution suggests that ErFeO₃ was characterized by four absorption bands, peaked at 1.84, 2.76, 3.4, and 4.6 eV indicated in Fig. 2(d). Small humps in the spectrum, which matched well with the literature,²⁹ are associated with the absorption bands of orthorhombic ErFeO₃. It is reported that the absorption peaks of orthorhombic ErFeO₃ are blue shifted compared to that of the hexagonal counterpart associated with stronger crystal field splitting at a Fe-O₆ cage.²⁸ In the case of hexagonal structure, the crystal contains a Fe-O₅ geometrical entity as a building structure, where an orthorhombic crystal is formed through the Fe-O₆ octahedral cage. The axial interaction of O p-orbitals with Fe d-orbitals in the case of an octahedral arrangement leads to the stronger crystal field splitting and thereby electronic levels occur at higher energies than that in the hexagonal counterpart. Rai *et al.*²⁸ found similar observations on YFeO₃. Absorption peaks of h-YbFeO₃ in their work occurred at 2.3, 2.9, 4.2, and 5.8 eV, whereas that of o-YbFeO₃ appeared at higher energies, e.g., at 2.7 eV corresponding to 2.3 eV for a h-structure.²⁸ Absorption peaks of h-ErFeO₃ are reported to occur at 2.23, 2.94, 3.77, and 5.08 eV.²⁹ By similar correlation of YFeO₃, the peaks at 2.76, 3.40, and 4.60 eV observed in the present work are associated with o-ErFeO₃. The higher energy absorption peak corresponding to 5.08 eV of the h-structure is possibly superimposed on the absorption saturation band of a glass substrate which commenced in Fig. 2(c) at 5.09 eV. Furthermore, these spectral characteristics correspond to specific transitions between different electronic energy bands of Fe, O, and Er atoms. The lower-energy peaks at 1.84 and 2.76 eV are due to the absorption transition between Fe d and d orbitals, whereas the one at 3.40 eV have contribution of charge transfer (CT) transition from the

valence band formed by the occupied 2p oxygen orbitals to the conduction band formed by unfilled 3d iron orbitals.^{36,37} The absorption band at a higher energy of 4.60 eV (and the one submerging into the saturation region) is purely due to CT transition between oxygen 2p and iron 3d orbitals. In the context of NL optical characterization, the absorption bands centered at 2.76 eV, 3.40 eV, and 4.60 eV suggest the possibility of 2PA at 600 nm, 2PA and 3PA at 800 nm and 1200 nm.

B. Nonlinear optical properties

The CA Z-scan data of ErFeO₃ film recorded with a low input intensity of 0.04 GW/cm² is shown in Fig. 3(a). The input power level was chosen to be very low to suppress the NLA effects. The normalized transmittance presented in the diagram is the ratio of Z-dependent transmitted power to the linear transmitted power; the linear one is measured keeping the sample far away from the focus where the NLA is absent. A “valley followed by peak”-type of CA response in the figure is the result of intensity-dependent NLR. The sharp increase in the transmittance close to the focus observed in Fig. 3(a) is associated with the increase in the sample’s refractive index with the increase of the light intensity. On moving the sample toward the focus, the laser beam bends toward the axis so that now more photons (increased intensity) are able to pass through the aperture window. Thus, the transmittance increases and the graph transforms from the valley to the peak type. The NLR parameters are evaluated by fitting the experimental data using Eq. (4).¹⁶ Fitted data are shown in the same figure by solid lines. The value of on-axis phase shift, $\Delta\theta_0$, the fit parameter, is estimated to be 0.65. The nonlinear refractive index, n_2 calculated using the defining relation of $\Delta\theta_0$, mentioned above, is 6.75×10^{-13} cm²/W, where the positive sign represents the focusing nature of the sample. This n_2 of ErFeO₃ value is found comparable to that of the thin film-ferrite, i.e., BiFeO₃, reported in the literature,³⁸ which under 780 nm femtosecond laser pulse excitation exhibited the NLR with $n_2 = 1.46 \times 10^{-13}$ cm²/W. Furthermore, order and purity (whether is of thermal origin) of the nonlinearity are also confirmed from the transmittance, i.e., the peak-valley, profile.¹⁶ The separation of peak to valley, ($\Delta Z_{p-v} = 6.00$ mm) equals to $1.7Z_R = 5.98$ mm confirms that the nonlinearity in the refraction is caused by the third order process, where the overall refractive index is given as $n = n_0 + n_2I$, with n_0 being the linear refractive index. It is wise to mention that a separation close to $1.2Z_R$ corresponds to a fifth order NL process, whereas ΔZ_{p-v} higher than $1.7Z_R$ suggests that the process may predominantly have dominance of the thermal effect.¹⁶ Again, ΔZ_{p-v} of 5.98 mm

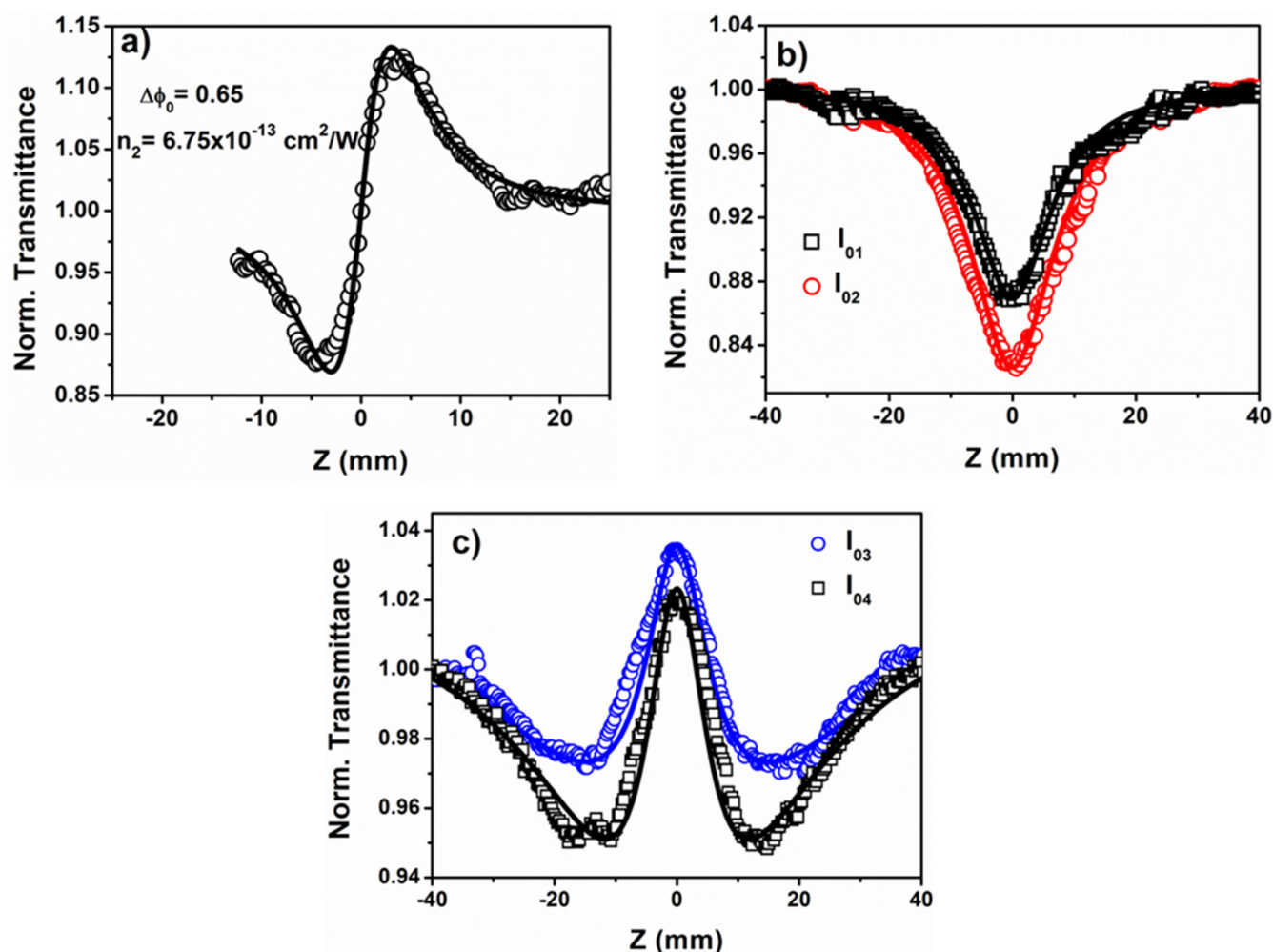


FIG. 3. Z-scan graph of solgel assisted spin coated ErFeO_3 film at 800 nm in (a) closed aperture configuration at an input intensity of 0.04 GW/cm^2 and in [(b) and (c)] open aperture at an input intensity of (b) $I_{01} = 0.13$ and $I_{02} = 0.18 \text{ GW/cm}^2$ and (c) $I_{03} = 0.49$ and $I_{04} = 0.66 \text{ GW/cm}^2$. Scattered symbols represent the experimental data where as solid lines correspond to the fitted data.

conveys that the origin of change in the refractive index is evidently not thermal in nature.

The OA Z-scan data of ErFeO_3 thin film were recorded at 800 nm at four input intensities of 0.13 GW/cm^2 , 0.18 GW/cm^2 , 0.49 GW/cm^2 , and 0.66 GW/cm^2 . The normalized transmittance data as a function of sample position with respect to lens' focal point (i.e., $Z=0$) are shown in Figs. 3(b) and 3(c). ErFeO_3 in Fig. 3(b) illustrates reverse saturable absorption (RSA) or valley-type behavior at lower input intensities of 0.13 and 0.18 GW/cm^2 where the sample transmittance drops continuously with increasing laser intensity, i.e., when the sample moves toward the focus. This valley-type response can be the result of multi-photon absorption (MPA)^{39–42} or ESA,^{42–44} both of which reduce the number of photons significantly in the transmitted beam. At a higher input

intensity of $I_{03} = 0.49 \text{ GW/cm}^2$, this RSA behavior gets limited to the off-focus region. The Z-scan graph turns to the SA-type (peak-type) in the near focus region for the saturation of the absorption process and thus transmittance is observed increasing on moving toward the focus. The NL effect of MPA or ESA is expected to saturate the same way as LA does on lacking the molecules at the initial state. The complete transmittance curve of Fig. 3(c) is collectively referred as SA-in-RSA or W-shape behavior,¹⁵ which consistently exists at a higher input intensity of 0.66 GW/cm^2 with a relatively wider spread over a Z-coordinate. Admitting the one photon absorption at 800 nm, the experimental data of Figs. 3(b) and 3(c) were fitted with the model containing the linear and instantaneous 2PA coefficients given by Eq. (16). In the case of Z-scan with short-lived laser pulses (e.g., femtosecond), the

transition from ES is almost instantaneous and the difference between ESA and 2PA is of least significance.²⁰ The molecules at 800 nm can be excited by 2PA involving transition between Fe d and d orbitals and CT transition between Fe d and O p-orbitals and pictorially to the upper part of band-S₁ and/or lower part of band-S₂ of Fig. 1 [since the absorption peaks at 2.76 and 3.40 eV are overlapped, Fig. 2(d)].^{36,37} The data are fitted with the model expression given by Eq. (16) taking the lifetime of excited states, S₁ and S₂, such that the ratio, $\eta_{12} = \tau_1/\tau_2 = 10$. The fitted curves are shown by the solid lines in the same figure. The Z-scan data at peak intensities of 0.13 GW/cm² and 0.18 GW/cm² were initially fitted with the model comprising 1PA and 2PA without any saturation effects (by setting $I_{S1}, I_{S2} \gg I_0, I_{00}$). The data did not fit satisfactorily to the experimental values. To fit better, one more process, the saturation of LA was included in the model [by taking the relatively finite value of I_{S1} in Eq. (16)]. The close match of the data with such a generalized model suggests the simultaneous presence of two NLA phenomena. The saturation effects however are such lower that the transmittance curve remains in the valley-shape and does not transform to the RSA-in-SA shape, which is commonly known as signature graphs of the 1PA saturation process.^{15,21} Saturation of LA is also a NL phenomenon which occurs due to the bleaching of the molecules at the ground energy state. At high intensities, the molecules spend longer time at the ES than at the GS and thus creating its deficit at the GS. Higher the intensity, more the deficit and higher will be the saturation and thus the transmission. Therefore, a competing “decreased absorption” increases the wideness of the RSA valley and reveals the ErFeO₃'s ability for smooth better control of the intensity in OL applications. Furthermore, these materials can be used in pulse-shaping applications. At higher input intensities, the saturation of 2PA is considered to fit near-focus saturation behavior. The estimated NL parameters β_0 , I_{S1} , and I_{S2} for all the four input intensities are quoted in Table II. It is observed that the β_0 -value increases on increasing the input intensity from 0.13 GW/cm² to 0.66 GW/cm². The change is for the involvement of more and more molecules in the 2PA with increasing intensity. The 2PA cross section is calculated using Eq. (10) except the instantaneous population density at GS (i.e., $N-N_1-N_2$) is replaced by the undepleted population density N . The value of N is calculated from the XRD data analysis and observed to be 8.04 g/cm³. It is common practice to consider

N , the undepleted concentration, for the calculation of cross section.²³ The 2PA saturation intensity, I_{S2} , for the cases of 0.3 and 0.4 GW/cm² follow a reverse trend of β_0 values as expected from the definition of I_{S2} ; I_{S2} is inversely proportional to σ_{2PA} . Conversely, σ_{1PA} (I_{S1}) under the saturation effect increases (decreases) when the input intensity increases from 0.18 to 0.49 and then to 0.66 GW/cm². As mentioned above, the absorption saturation is caused by the bleaching of the molecules in the GS. The molecules excited to SES by 2PA get de-excited to the original state in a shorter time compared to the molecule which is excited to the FES by 1PA. With the increase in the input intensity, as more molecules involve in the 2PA, 1PA might be facilitated by these de-excited molecules, thereby leading to an increase in σ_{1PA} and a decrease in I_{S1} . A decrease in I_{S1} (when defined in the same way^{21,23}) on increasing the input power is reported for other compositions also.²¹ Overall, the transmittance curve and the NLO parameters of ErFeO₃ at $\lambda_{exc} = 800$ nm suggest that 2PA and saturation of 1PA can occur simultaneously while preserving the RSA behavior. ErFeO₃ can still be used for OL applications at input intensities in the range of 0.13–0.18 GW/cm². On the other hand, with W-shape, the optical limiting (OL) application can be of selective nature where a range of intensities will be blocked by the material while out of the range will be allowed.

The OA Z-scan experiments were also performed at the wavelengths of 600 nm and 1200 nm, whose recorded graphs are shown in Figs. 4(a) and 4(b), respectively. ErFeO₃ film, similar to the 800 nm-case, exhibited RSA characteristics at 600 nm. This RSA characteristic sustains at the three inputs of $I_{01} = 0.21$ GW/cm², $I_{02} = 0.43$ GW/cm², and $I_{03} = 0.66$ GW/cm², in the systematically increasing degree with the input intensity associated with the increase in the NLA cross section.¹⁵ Under the same experimental conditions (initial beam spot size and converging lens focal length), the transmittance at 600 nm was observed to drop faster with respect to sample position (i.e., intensity) compared to the one at 800 nm, thereby giving a narrower appearance to the overall RSA response; this narrowness to a certain degree is related to Rayleigh length, Z_R , thereby laser intensity profile, $I(Z) (= I_{00}/\{1 + (Z/Z_R)^2\})$; Z_R changes from 6.08 mm to 4.56 mm. The RSA or OL characteristic is primarily associated with 2PA caused by the CT transition from Fe d-orbital to O p-orbital (and to the level S₃ in Fig. 1). Absorption by two photons is also reflected in

TABLE II. NLA parameters of solgel assisted spin coated ErFeO₃ films estimated from the fs Z-scan experiments at excitation wavelengths of 600 nm, 800 nm, and 1200 nm. GM—Goppert-Mayer unit of two-photon absorption cross section, 1 GM = 10⁻⁵⁰ cm⁴s

| λ (nm) | I_0 (GW/cm ²) | I_{S1} (W/cm ²) | β_0 (cm/W), σ_{2PA} (GM) | I_{S2} (W/cm ²) |
|----------------|-----------------------------|-------------------------------|---------------------------------------|-------------------------------|
| 600 | 0.21 | 8×10^{14} | 6.9×10^{-10} , 1.28 | ... |
| | 0.43 | 8×10^{14} | 8.5×10^{-10} , 1.58 | ... |
| | 0.66 | 3×10^{13} | 9.7×10^{-10} , 1.80 | ... |
| 800 | 0.13 | 4.00×10^{11} | 2.38×10^{-8} , 33 | ... |
| | 0.18 | 4.50×10^{11} | 2.50×10^{-8} , 35 | ... |
| | 0.49 | 5.51×10^{10} | 1.04×10^{-7} , 145 | ... |
| | 0.66 | 1.95×10^{10} | 2.75×10^{-7} , 383 | 9.35×10^{11} |
| 1200 | 3.47 | ... | 5.80×10^{-13} , 0.5 mGM | ... |
| | 5.26 | ... | 1.98×10^{-12} , 1.84 mGM | 9×10^{11} |

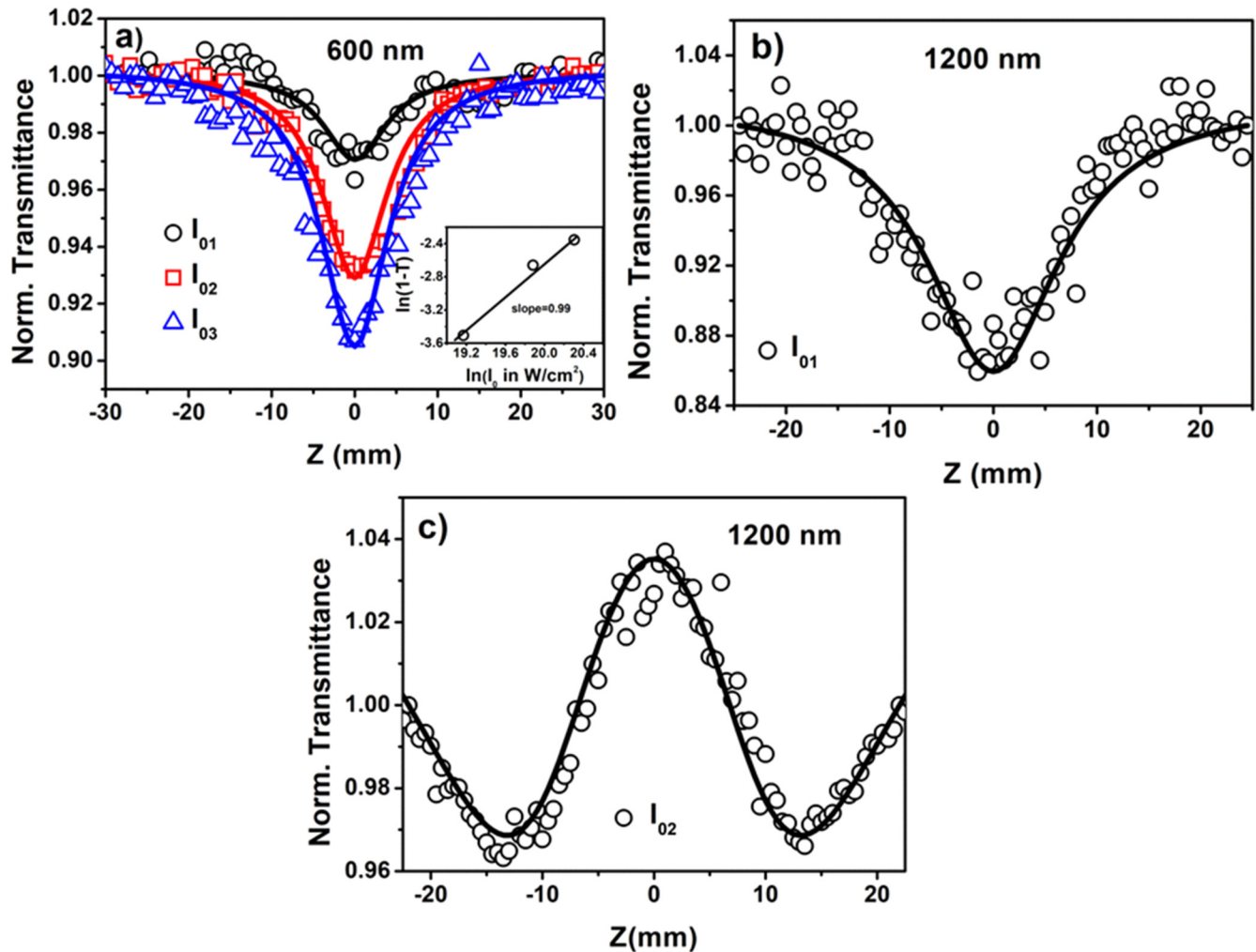


FIG. 4. Open aperture z-scan graph of sol-gel assisted spin coated ErFeO_3 films at (a) 600 nm and (b) 1200 nm. Scattered symbols represent the experimental data, whereas solid lines correspond to fitted ones.

the linearity of \log_e of the on-axis transmittance at the focus vs \log_e of input intensity with a slope close to 1; higher slopes of 2, 3, 4, and so on corresponds to higher order multi-photon absorption processes.⁴¹ The valley-type data similar to the 800 nm-case are fitted by the model expression given by Eq. (16) involving linear absorption [$S_0 \rightarrow S_1$, refer to Fig. 2(b)] and 2PA ($S_0 \rightarrow S_3$) with $\eta_{13} = \tau_1/\tau_3 = 100$. The fitted graph is shown in the same as Fig. 4(a) with solid lines and the estimated NL parameters are listed in Table II. The NLA coefficient of ErFeO_3 at $\lambda_{\text{exc}} = 600$ nm is of the order of 10^{-10} cm/W, 1–2 orders of magnitude lower than that obtained at 800 nm. The observed decrease in the absorption coefficient suggests that it is not only the LA at $\lambda_{\text{exc}}/2$ that governs the NLA or MPA (discussed again at a later stage). 2PA cross-section not following the trend of LA is reported by Olesiak-Banska *et al.* for Au-nanoparticles.²³ The 2PA coefficient systematically

increased from 6.9×10^{-10} cm/W to 9.7×10^{-10} cm/W for a change of the input intensity from 0.21 GW/cm² to 0.66 GW/cm². The RSA curve at the highest input intensity is fitted with the 1PA saturation to define correctly the wideness of the valley.

NLA characteristics at 1200 nm on the other hand could have recorded at relatively higher input intensities. The OA Z-scan graph is shown in Figs. 4(b) and 4(c) at two input intensities of 3.48 and 5.26 GW/cm². ErFeO_3 at $\lambda_{\text{exc}} = 1200$ nm demonstrated RSA behavior at the 3.48 GW/cm² and W-type strong saturation at 5.26 GW/cm². Significantly wider RSA characteristics, spread over (-25 mm, 25 mm), is due to the higher Z_R at 1200 nm. The experimental data were fitted with 2PA and negligible LA [Eq. (17)]. β_0 in this case is observed to be of the order of 10^{-13} with the value of 7.3×10^{-13} at 1.89 GW/cm². Smaller absorption coefficient is associated with the low LA ability at $\lambda_{\text{exc}}/2$, i.e., 600 nm

[Fig. 2(b)]. At higher input intensity, the strong absorption saturation is characterized by an absorption coefficient of 1.98×10^{-12} cm/W and saturation intensity of 9×10^{11} W/cm². Like the previous cases, though the absorption saturates, the NLA coefficient and thus the absorption cross section increases with the intensity. We expect an error of $\pm 10\%$ in the NLO coefficients presented in this work due to the input power fluctuations, error in the estimation of beam waist and other fitting errors, etc. We also checked the contribution from the substrate alone and it was found to be negligible.

Regarding the wavelength dependent collective picture of the 2PA characteristics of the materials, it is reported that the

bands become highly non-parabolic at 2PA particularly when $2h\nu$ is significantly greater than E_g . In this case, the 2PA coefficient is given as⁴⁵

$$\beta_0 = 4\pi \left(\frac{e^4}{\hbar c^2} \right) \left(\frac{P}{n^2 E_g^3} \right) f \left(\frac{h\nu}{E_g} \right).$$

All the terms hold standard definition, except P is a constant, ω and n are angular frequency and refractive index at the radiation frequency and f defines the band structure and is a function of $h\nu/E_g$. For non-parabolic model-case f is given as

$$f(\alpha) = \frac{(2\alpha - 1)^{1.5}}{\alpha^3} \left[\frac{4}{45} 3^{1.5} (4\alpha - 1) \alpha^{1.5} \left\{ \left(\frac{2}{\alpha} - \frac{1}{3\alpha - 1} \right)^2 + \frac{1}{(3\alpha - 1)^2} \right\} + \frac{2}{15} \left(\frac{3}{2} \right)^{1.5} \alpha (2\alpha + 1)^{1.5} \right],$$

where $\alpha = h\nu/E_g$. This relation in the same paper was used to compare the β -values of semiconductors (having bandgap E_g , which satisfies the condition $E_g/2 < h\nu < E_g$ at the excitation frequency) considering non-parabolic model of bands. Later, this relation was applied to a series of semiconductors⁴⁶ by Stryland to show that β (normalized over band function f and the constant P) at a specific wavelength varies as inverse of cube of E_g . In other work, β of ZnO was shown to change with Ni doping for change in the bandgap following the above relation.⁴⁷ These works are dedicated to the comparison of β of materials having closely related bandgaps and excited by a common source/wavelength. On the other side, Wei *et al.* in a wavelength dependent study showed that β of $\text{CH}_3\text{NH}_3\text{PbX}_3$ (X: Cl, Br, I) varies from 2.5×10^{-4} cm/MW to 272 cm/MW for a change of f -parameter ($h\nu/E_g$) from 0.524 to 0.76 following the above equation.⁴⁸ In the present case, the measurements are performed at different wavelengths which excite the ErFeO_3 system to different allowed energy bands as shown in Fig. 1. Different bands are characterized with different bandgaps and band structure parameters. Also, because of overlapping absorption peaks in the absorption spectrum [Fig. 2(d)], it was difficult to determine band edge (and bandgap) using a Tauc plot [a graph between $(\alpha h\nu)^2$ and $h\nu$].⁴⁹ It is therefore rather complicated to draw a conclusion of the wavelength dependent NLA coefficient involving different bands. However, it is expected that different band-structure parameter can be one of the primary reasons for observed changes in the 2PA coefficients at 600 ($h\nu/E_{g600} = 0.45$) and 800 ($h\nu/E_{g800} = 0.46$ for 3.4 eV and 0.56 for 2.76 eV) excitation wavelengths where E_g 's are taken from the absorption peaks [Fig. 2(d)].

Here, we also present a comparison of 2PA coefficients of few oxide ceramics. A similar composition YCrO_3 , in a powder form, dissolved in ethylene glycol exhibited 3PA at 532 nm, with γ -absorption coefficient of 6.3×10^{-24} m³/W². 3PA absorption of YCrO_3 is derived from 2PA involving CT transition (similar to ErFeO_3 of the present work, at relatively closer $\lambda_{\text{exc}} = 600$ nm). Prior to another photon absorption, the YCrO_3 system is reported

to undergo a radiative decay transition to a metastable state which acted as the initial state for ESA. BaTiO_3 powders dissolved in ethylene glycol exhibited grain size dependent 2PA at 532 nm with $\beta = 11.0 \times 10^{-9}$ cm/W and 6.0×10^{-9} cm/W for grain sizes of 16 nm and 26 nm, respectively.⁵⁰ As an example to the NLO study of thin films, $\text{Ba}_{0.5}\text{Sr}_{0.5}\text{TiO}_3$ (BST)⁵¹ exhibited 2PA at $\lambda_{\text{exc}} = 800$ nm with $\beta = 1.6 \times 10^{-10}$ cm/W at the peak intensity of 2.0×10^{11} W/cm². The absorption characteristics of BST changed to 3PA with an increase of film deposition temperature that essentially enhanced the crystallinity of the film. However, in the present case of ErFeO_3 , with a relatively lower peak intensity of 1.03×10^{11} – 1.44×10^{11} W/cm², the absorption coefficient is two orders higher than that of the BST film. This change may be associated with the higher (theoretical) density of ErFeO_3 film and higher LA coefficient at $\lambda_{\text{exc}}/2$.⁵² Furthermore, we compare the NLA characteristics of ErFeO_3 with one of the widely reported strong NLO ceramic oxides, i.e., zinc oxide. NLO property of ZnO has been studied in various forms: colloidal solution of bulk powder, thin film, and composite, at different wavelengths of 532 nm, 633 nm, and 800 nm, etc. Min *et al.*⁵³ has reported a Z-scan study of ZnO nanorods of 400 nm length and 100 nm diameter grown on an indium titanium oxide (ITO) substrate by electro-deposition. 2PA coefficient at $\lambda_{\text{exc}} = 800$ nm was observed to be 2.3×10^{-7} cm/W at 1.2 GW/cm². Lee *et al.* also reported a Z-scan of 1 μm long ZnO nanorods grown on an ITO substrate at 800 nm and β was 1.0×10^{-6} cm/W with no mention of input intensity/power.⁵⁴ Maung *et al.*⁵⁵ recorded a Z-scan of ZnO films of thickness of 2 μm at 532 nm and β as 4.86×10^{-5} cm/W at 0.265 GW/cm². Irimpan *et al.*⁵⁶ found 2PA in ZnO films deposited on glass at 532 nm with β of 4.59×10^{-3} cm/W at 0.22 GW/cm². Higher β -value in this particular case seems partly associated with the large thickness of the sample since the absorbance of the sample was >2 and more significantly involved nanosecond excitation probably invoking excited state absorption (not pure two-photon absorption). Rana *et al.*⁴⁷ found β of Ni doped ZnO nanorods dispersed in ethanol to be 7.6×10^{-9} cm/W and 1.12×10^{-7} cm/W for the rod lengths of 100

and 200 nm corresponding to the doping level of 0 and 10 mol. %, respectively. The measurements were performed at 532 nm with an input intensity in the range of 0.1–0.3 GW/cm². The β -increase was associated with the changes in the bandgap by Ni doping. Collectively, the β -value of ZnO at 532 nm is 2–3 orders higher than that at 800 nm though the NLA coefficient does not appear to be significantly different.⁴⁷ In comparison, β of ErFeO₃ thin films is comparable to that of ZnO at 800 nm and slightly lower at 600 nm.

The effect of preferred orientation on the NLO properties can be important for films and confined structures.^{53,54} For example, 100 and 500 nm diameter nanorods of zinc oxide exhibit 2PA with coefficient, β , of 2.3×10^{-7} and 5.9×10^{-7} cm/W, respectively.^{50,53} If a Z-scan is recorded on a sample having oriented grains, the transmittance at λ_{exc} can be different from the one with differently or non-oriented grained samples. This change in the NLO will be brought up by the variation in the bandgap, thereby the absorption characteristics. In the present case, due to the polycrystalline nature and $\sim 1 \mu\text{m}$ thickness of the film (confirmed from the Powder diffraction in a conventional θ – 2θ configuration), the anisotropy derived by a two-dimensional film-structure is believed to be minimum or insignificantly small. However, one may also expect preferred orientation in ErFeO₃ to result during a Z-scan from the magnetic field linked with the laser beam itself. The strength of the magnetic field can be really significant in high intensity laser pulses.⁵⁷ To speculate about the anisotropic effect, we need to re-examine the used Z-scan experimental condition (laser polarization state and incubation/existing time) and the magnetic property of ErFeO₃. Z-scan graphs have been recorded with a plane polarized laser beam having electric and magnetic field vectors predominantly confined in the plane of the film. The domain orientation by this linked magnetic field, if occurs, therefore will be confined in the plane of the film. Furthermore, the Z-scan experiment lasted for approximately 10 min and similar time was given as a gap to the next Z-scan run. Along with this, during the scan, the ferrite film sample experiences pulsed optical signal of 50 fs duration at the repetition rate of 1 kHz. Thus, during one second (10 min) of time, the magnetic field was available only for ≈ 50 ps (3 ns) which is really short for any significant domain orientation. Furthermore, ErFeO₃ at room temperature exhibits a narrow M–H hysteresis loop with small coercive field and remnant magnetization. The magnetization does not saturate but keeps on increasing with field at higher intensities due to its AFM characteristic.⁵⁸ Under all above mentioned experimental conditions, we expect the preferential domain orientation due to laser-linked magnetic field and thus caused anisotropy in the NLO properties to be low or negligible. Also, we had performed Z scan 2–3 times at each input intensity. If in one run, the ErFeO₃ sample underwent preferred orientation, the next run might have change in the transmittance. However, we did not observe significant changes in the transmittance. Also, we have recorded the Z-scan graphs (Figs. 3 and 4) in the increasing order of input intensity so that low intensity experiments were not affected by the magnetic history of the sample. However, it also might be possible that changes in the transmittance due to such anisotropic effect are small and of the same order that occurs by small fluctuations in power and therefore, cannot be distinguished. It is also reported in the literature⁵⁹ that a Z-scan performed with

different polarizations state (linearly, circularly, and elliptically) resulted into only small changes in the transmittance. The scan was performed on a dye sample with Ar-laser beam.⁵⁹

V. CONCLUSIONS

In summary, the present work demonstrates the use of solgel assisted spin coated $1 \mu\text{m}$ thick ErFeO₃ films as a reverse saturable absorber at the wavelengths of 600 nm, 800 nm, and 1200 nm. The structural properties of the deposited film were confirmed by the x-ray diffraction and micro-Raman spectroscopic techniques. The NLO properties of ErFeO₃ film sample were characterized by femtosecond Z-scan experiments at different intensities at three excitation wavelengths of 600 nm, 800 nm, and 1200 nm. The optical nonlinearity of ErFeO₃ is mainly of the third-order caused by 2PA which is shown to be saturated at the higher intensities at both 800 nm and 1200 nm. A generalized theory is developed for three simultaneously occurring processes, i.e., 1PA, 2PA, and ESA (2PA, 3PA, and ESA2) along with their saturation. These equations are shown to turn to simple models, e.g., hyperbolic for the saturation of linear absorption in a homogeneously broadened system, in the limiting conditions. The optical limiting characteristic of ErFeO₃, which exists at all these wavelengths, demonstrated the best performance at 800 nm. It is suggested that RSA characteristics preserved under the absorption saturation have potential for better controlling or limiting the higher input peak intensities.

REFERENCES

- ¹C. H. Tsang, R. L. White, and R. M. White, *AIP Conf. Proc.* **29**, 552 (1976).
- ²S. Konishi, T. Miyama, and K. Ikeda, *Appl. Phys. Lett.* **27**, 258 (1975).
- ³R. L. White, *J. Appl. Phys.* **40**, 1061 (1969).
- ⁴J. A. De Jong, A. V. Kimel, R. V. Pisarev, A. Kirilyuk, and T. Rasing, *Phys. Rev. B* **84**, 104421 (2011).
- ⁵A. V. Kimel, A. Kirilyuk, P. A. Usachev, R. V. Pisarev, A. M. Balbashov, and T. Rasing, *Nature* **435**, 655 (2005).
- ⁶R. V. Mikhaylovskiy, E. Hendry, V. V. Kruglyak, R. V. Pisarev, T. Rasing, and A. V. Kimel, *Phys. Rev. B* **90**, 184405 (2014).
- ⁷K. Yamaguchi, T. Kurihara, Y. Minami, M. Nakajima, and T. Suemoto, *Phys. Rev. Lett.* **110**, 137204 (2013).
- ⁸S. Krishnan, K. Shafakath, R. Philip, and N. Kalarikkal, *AIP Conf. Proc.* **1576**, 138–140 (2014).
- ⁹S. Krishnan, C. S. S. Sandeep, R. Philip, and N. Kalarikkal, *Chem. Phys. Lett.* **529**, 59 (2012).
- ¹⁰D. J. Harter, M. L. Shand, and Y. B. Band, *J. Appl. Phys.* **56**, 865 (1984).
- ¹¹D. Swain, P. T. Anusha, T. S. Prashant, S. P. Tewari, T. Sarma, P. K. Panda, and S. Venugopal Rao, *Appl. Phys. Lett.* **100**, 141109 (2012).
- ¹²Y. B. Band, in *Methods in Laser Spectroscopy*, edited by Y. Prior, A. Ben-Reuven, and M. Rosenbluh (Springer, Boston, MA, 1986), pp. 117–121.
- ¹³B. Q. Z. Han, N. Zhenhua, W. Yu, P. Lakshminarayana, S. Zexiang, X. Qing-Hua, T. Y. Ding, and L. K. Ping, *Nano Res.* **4**, 297 (2011).
- ¹⁴Y. I. Jhon, J. Koo, B. Anasori, M. Seo, J. H. Lee, Y. Gogotsi, and Y. M. Jhon, *Adv. Mater.* **29**, 1 (2017).
- ¹⁵A. Gaur, H. Syed, B. Yendeti, and V. R. Soma, *J. Opt. Soc. Am. B* **35**, 2906 (2018).
- ¹⁶M. Sheik-Bahae, A. A. Said, T.-H. Wei, D. J. Hagan, and E. W. Van Stryland, *IEEE J. Quantum Electron.* **26**, 760 (1990).

- ¹⁷A. S. Reyna, I. Russier-Antoine, F. Bertorelle, E. Benichou, P. Dugourd, R. Antoine, P.-F. Brevet, and C. B. De Araujo, *J. Phys. Chem. C* **122**, 18682 (2018).
- ¹⁸S. M. Kirkpatrick, R. R. Naik, and M. O. Stone, *J. Phys. Chem. B* **105**, 2867 (2001).
- ¹⁹B. Gu, J. He, W. Ji, H. Wang, B. Gu, J. He, W. Ji, and H. Wang, *J. Appl. Phys.* **103**, 073105 (2008).
- ²⁰S. V. Rao, D. N. Rao, J. A. Akkara, B. S. DeCristofano, and D. V. G. L. N. Rao, *Chem. Phys. Lett.* **297**, 491 (1998).
- ²¹S. Hamad, S. P. Tewari, L. Giribabu, and S. V. Rao, *J. Porphyr. Phthalocyanines* **16**, 140 (2012).
- ²²B. Gu, W. Ji, P. S. Patil, S. M. Dharmaparakash, and H. T. Wang, *Appl. Phys. Lett.* **92**, 091118 (2008).
- ²³J. Olesiak-Banska, M. Waszkielewicz, K. Matczyszyn, and M. Samoc, *RSC Adv.* **6**, 98748 (2016).
- ²⁴C. Torres-Torres, J. Bornacelli, B. Can-Uc, H. G. Silva-Pereyra, L. Rodeiguez-Fernández, M. Borja-Avalos, G. J. Labrada-Delgado, J. C. Cheang-Wong, R. Rangel-Rojo, and A. Oliver, *J. Opt. Soc. Am. B* **35**, 1295 (2018).
- ²⁵H. Sánchez-Esquivel, K. Y. Raygoza-Sanchez, R. Rangel-Rojo, B. Kalinic, N. Michieli, T. Cesca, and G. Mattei, *Nanoscale* **10**, 5182 (2018).
- ²⁶R. Rangel Rojo, S. Yamada, H. Matsuda, H. Kasai, H. Nakanishi, A. K. Kar, and B. S. Wherrett, *J. Opt. Soc. Am. B* **15**, 2937 (1998).
- ²⁷M. Alam, I. Chakraborty, and K. Mandal, *J. Lumin.* **196**, 387 (2018).
- ²⁸R. C. Rai, C. Horvatits, D. McKenna, and J. Du Hart, *AIP Adv.* **9**, 015019 (2019).
- ²⁹V. V. Pavlov, A. R. Akbashev, A. M. Kalashnikova, V. A. Rusakov, A. R. Kaul, V. V. Pavlov, A. R. Akbashev, A. M. Kalashnikova, V. A. Rusakov, and A. R. Kaul, *J. Appl. Phys.* **111**, 056105 (2012).
- ³⁰S. Venugopalan, M. Dutta, A. K. Ramdas, and J. P. Remeika, *Phys. Rev. B Condens. Matter Mater. Phys.* **31**, 1490 (1985).
- ³¹N. Koshizuka and S. Ushida, *J. Phys. Rev. B* **22**, 5394 (1980).
- ³²H. C. Gupta, M. K. Singh, and L. M. Tiwari, *J. Raman Spectrosc.* **33**, 67 (2002).
- ³³M. C. Weber, M. Guennou, H. J. Zhao, J. Íñiguez, R. Vilarinho, A. Almeida, J. A. Moreira, and J. Kreisel, *Phys. Rev. B* **94**, 214103 (2016).
- ³⁴M. Marezio, J. P. Remeika, and P. D. Dernier, *Acta Crystallogr. Sect. B Struct. Crystallogr. Cryst. Chem.* **26**, 2008 (1970).
- ³⁵E. Kroumova, M. L. Aroyo, J. M. Perez-Mato, A. Kirov, C. Capillas, S. Ivantchev, and H. Wondratschek, *Phase Transit.* **76**, 155 (2003).
- ³⁶P. A. Usachev, R. V. Pisarev, A. M. Balbashov, A. V. Kimel, A. Kirilyuk, and T. Rasing, *Phys. Solid State* **47**, 2292 (2005).
- ³⁷R. V. Pisarev, A. S. Moskvina, A. M. Kalashnikova, and T. Rasing, *Phys. Rev. B Condens. Matter Mater. Phys.* **79**, 1 (2009).
- ³⁸G. Bing and W. Hui-Tian, in *Ferroelectrics—Physical Effects* (IntechOpen, 2011), pp. 506–526.
- ³⁹S. Chen, M.-L. Zheng, X.-Z. Dong, Z.-S. Zhao, and X.-M. Duan, *J. Opt. Soc. Am. B* **30**, 3117 (2013).
- ⁴⁰B. Gu, Y. X. Fan, J. Chen, H. T. Wang, J. He, and W. Ji, *J. Appl. Phys.* **102**, 083101 (2007).
- ⁴¹J. He, Y. Qu, H. Li, J. Mi, and W. Ji, *Opt. Express* **13**, 9235–9247 (2005).
- ⁴²M. Chattopadhyay, P. Kumbhakar, C. S. Tiwary, A. K. Mitra, U. Chatterjee, and T. Kobayashi, *Opt. Lett.* **34**, 3644 (2009).
- ⁴³N. Venkatram, D. Narayana Rao, L. Giribabu, and S. Venugopal Rao, *Chem. Phys. Lett.* **464**, 211 (2008).
- ⁴⁴Q. Bellier, N. S. Makarov, P. A. Bouit, S. Rigaut, K. Kamada, P. Feneyrou, G. Berginc, O. Maury, J. W. Perry, and C. Andraud, *Phys. Chem. Chem. Phys.* **14**, 15299–15307 (2012).
- ⁴⁵C. R. Pidgeon, B. S. Wherrett, A. M. Johnston, J. Dempsey, and A. Miller, *Phys. Rev. Lett.* **42**, 1785 (1979).
- ⁴⁶E. W. Van Stryland, M. A. Woodall, H. Vanherzeele, and M. J. Soileau, *Opt. Express* **10**, 490 (1985).
- ⁴⁷A. K. Rana, J. Aneesh, Y. Kumar, M. S. Arjunan, K. V. Adarsh, S. Sen, and P. M. Shirage, *Appl. Phys. Lett.* **107**, 231907 (2015).
- ⁴⁸Z. Wei, D. Guo, J. Thieme, C. Katan, T. J. Savenije, V. M. Caselli, and J. Even, *Nat. Commun.* **10**, 5342 (2019).
- ⁴⁹J. Tauc, *Mater. Res. Bull.* **3**, 37 (1968).
- ⁵⁰T. Woldu, B. Raneesh, P. Sreekanth, M. V. R. Reddy, R. Philip, and N. Kalarikkal, *Chem. Phys. Lett.* **625**, 58 (2015).
- ⁵¹K. V. Saravanan, K. C. J. Raju, M. G. Krishna, S. P. Tewari, and S. V. Rao, *Appl. Phys. Lett.* **96**, 4 (2010).
- ⁵²S. Behera and A. Khare, *AIP Conf. Proc.* **2082**, 040006-1–040006-4 (2019).
- ⁵³S. Min, C. Oh, G. J. Lee, and Y. Lee, *J. Korean Phys. Soc.* **55**, 1005 (2009).
- ⁵⁴G. J. Lee, Y. Lee, H. Lim, H. Cheong, B.-H. Kil, and S.-H. Han, *J. Korean Phys. Soc.* **58**, 1290 (2011).
- ⁵⁵Z. Maung, Y. Zhang, C. Yao, H. Li, H. Li, and P. Yuan, *Opt. Mater.* **52**, 6 (2016).
- ⁵⁶L. Iriripan, A. Deepthy, B. Krishnan, and L. M. Kukreja, *Opt. Commun.* **281**, 2938 (2008).
- ⁵⁷M. Tatarakis, F. N. Beg, S. Diego, R. G. Evans, S. Peter, and D. Mangles, *Phys. Rev. E* **70**, 026401 (2004).
- ⁵⁸N. Ramu, R. Muralidharan, K. Meera, and Y. H. Jeong, *RSC Adv.* **6**, 72295 (2016).
- ⁵⁹P. D. Mohan and R. Dhar, *J. Laser Phys.* **23**, 125401 (2013).